Pore-scale simulation of laminar flow through porous media

# Pore-scale simulation of laminar flow through porous media

**M. Piller[1], D. Casagrande[2], G. Schena[1] and M. Santini[2]**

[1] Dipartimento di Ingegneria e Architettura, Università degli Studi di Trieste, via A. Valerio, 6/1 - 34127 Trieste, Italy

[2] Dipartimento di Ingegneria, Università degli Studi di Bergamo, viale Marconi, 5 - 24044 Dalmine (BG), Italy

E-mail: [1] `piller@units.it`

**Abstract.** The experimental investigation of flow through porous media is inherently difficult due to the lack of optical access. The recent developments in the fields of X-ray micro-tomography (micro-CT hereafter), digital sample reconstruction by image-processing techniques and fluid-dynamics simulation, together with the increasing power of super-computers, allow to carry out pore-scale simulations through digitally-reconstructed porous samples. The scientific relevance of pore-scale simulations lies in the possibility of *upscaling* the pore-level data, yielding volume-averaged quantities useful for practical purposes. One of the best-known examples of upscaling is the calculation of absolute and relative permeability of reservoir rocks. This contribution presents a complete work-flow for setting up pore-scale simulations, starting from the micro-CT of a (in general small) porous sample. Relevant applications are discussed in order to reveal the potential of the proposed methodology.

## 1. Introduction

The experimental investigation of flow through porous media is inherently difficult due to the lack of optical access. High resolution computed tomography allows to construct a digital binary model representing the complex pore space geometry. This three-dimensional synthetic model can be used for pore-scale simulations of phenomena that previously were often approached with macro-scale lumped models or micro-scale simplified models. Fluid flow through porous media is relevant in a range of industrial applications. In reservoir evaluation, absolute and relative permeabilities and capillary pressure are probably the most important flow properties for the set-up of reservoir simulations and for devising exploitation scenarios [1, 2]. The numerical calculation of these quantities mimics the protocols that are routinely used for experimental measurements.

Open-cell metal foams provide another example of porous media of practical relevance. They are characterised by a large specific surface area and, because of that, are used in many practical applications, as enhanced heat transfer devices [3, 4] and compact heat exchangers [5], catalytic reactors [6, 7], rotors of centrifugal compressors [8]. Open-cell metal foams have been investigated experimentally, analytically and numerically.

Pore-scale simulations of porous media are relatively novel. Mostaghimi et al. [9] simulate low-Reynolds-number flow and transport through digital samples of rock cores at the scale of pores, using a finite-difference solver. The absolute hydraulic permeability and the longitudinal dispersion coefficient are calculated. The same method is used to compute the permeability of a range of consolidated and unconsolidated porous rocks [10]. Boomsma et al. [11] carry out numerical simulations of laminar

flow through a cluster of two unit cells, each consisting of eight idealized pores of an open cell metal foam. A finite-volume method (FVM hereafter) is used to solve the incompressible, steady Navier-Stokes equations through the cell complex, using tetrahedral, unstructured meshes. Krishnan et al. [12] carry out pore-scale numerical simulations of both flow and heat transfer through an idealized, cubic unit cell, yielding good agreement with experimental data for foams with porosity larger than 94%. Gerbaux et al. [13] reconstruct digital samples of three open-cell metallic foams from X-ray tomography. Various unstructured, tetrahedral or cubic meshes are constructed. The microscopic Stokes flow through the foams is solved by two node-based FVM algorithms and one D3Q19 Lattice Boltzmann Method. The numerically computed and experimentally measured hydraulic permeabilities are in good agreement with each other and with available literature data. Bai et al. [4] carry out pore-scale numerical simulations for predicting the hydraulic head loss caused by a metal foam. They claim that the repetitive structure of metal foams allows for consideration of a single, idealized, representative unit cell, obtained by subtracting a sphere from a tetrakaidecahedron (sphere-centred Kelvin cell).

This study presents in detail a possible approach to the pore-scale flow simulation in digital porous systems reconstructed by X-ray computed tomography of real porous samples. Pore-scale numerical simulations are applied in three different studies, reported in the paper:

- Calculation of the absolute permeability tensor of samples of reservoir rocks.
- Calculation of both the relative permeability and the capillary pressure for laminar oil/water flow through a sample of sandstone rock.
- Investigation of the laminar flow through a sample of open-cell metal foam produced by infiltration casting [14, 15], within both the Darcy and the Darcy-Forchheimer regimes.

## 2. Materials and methods

### 2.1. X-ray computed tomography

Porous media are opaque to visible light which limits the measurements of their complex morphology often made up of stubby pores connected by narrower throats. The opacity prevents also the direct visualization of all the important phenomena related to the flow of multiphase fluids in the complex porous morphology. Among the tomographic imagining techniques, the X-ray computed tomography is the one with highest spatial resolution, good penetrating capability and thus it is the most suited for the morphological reconstruction of porous media samples with micrometric throats. Today the micrometric resolution obtainable at the tomographic beam-lines of synchrotron facilities is possible with micro- and nano-CT laboratory tomographic machines based on open-type cone-beam tubes. These tubes can focus the X-ray beam to less than 1 micron spot size and allow the production of a Bremsstrahlung (i.e. polychromatic and incoherent) X-ray beam with energies suitable for micrometric spatial resolution tomography in a millimetric size sample. A typical X-ray tomography station is made up with a planar digital detector (either CCD arrays or flat panels are used to capture intensity data after X-ray to visible light conversion on a scintillator) and a high precision rotating stage. The object is placed on the stage and rotated by small angular steps, a radiographic operation is repeated at each step. The collection of radiographies is made up of several hundreds of projections depending on the diameter of the object. The radiographic principle is conceptually simple: X-rays traverse a cross section of the sample along straight lines, the intensity of the attenuated X-ray signal emerging is converted by a scintillator into light and recorded as a digital image. The X-ray attenuation obeys the Beer-Lambert law that states that there is a logarithmic dependence between the transmission of a ray through an object and the distance it travels :

$$\ln\left(\frac{I_o}{I_i}\right) = \int_L \mu\left(l, E\right) \, \mathrm{d}l \tag{1}$$

where $\mu$ is the linear attenuation coefficient of the material, $I_o$ is the intensity of the incident impinging X-ray beam, $I_i$ is the intensity emerging from the object and L is the material thickness that is the distance

travelled. The linear attenuation coefficient is a function of the photon energy $E$. The incident intensity is read on the so called flat-field that is the radiography taken without sample before starting an acquisition. The logarithm of the intensity ratio is also referred to as projection. It contains an integral (through the length travelled in the material) information about the attenuation properties encountered by the ray. This information should be de-convoluted to extract information about the local internal (morphology) of the material.

*2.1.1. Filtered back projection and segmentation*   The mathematical principle of the CT reconstruction for parallel rays was developed early in the last century by Radon et al. [16]. The Radon inverse recreates the map of the linear attenuation coefficients of the object cross-section from the collection of projections taken around it (i.e., from the *sinogram*). The process can be seen as a filtration of the projection in the Fourier domain and a back projection into the pixels of the image grid. The whole operation is often referred to as filtered back projection (FBP). The algorithm generalizing in 3D the Radon inverse for diverging cone-beams is due to Feldkamp et al. [17] and is also cast around the original filtered back projection technique.

*2.1.2. Example of a home-made X-ray tomography devices*   The X-ray micro-tomographic facility available to the authors at University of Bergamo is based on an open type Hamamatsu X-ray source 160 kVp. An Aerotech rotary air-bearing drive stage provides superior angular positioning and velocity stability. The X-ray projections are collected by a Dexela-Perkin Elmer 1512 flat panel Complementary Metal-Oxide-Semiconductor (CMOS) X-ray detector. The detector has a pixel size of 75 micron and allows binning. The frame rate is 30fps at full resolution. The cabinet has 5 mm of lead shielding. To mitigate the effect of the beam hardening on imaging a thin aluminium filter plate is used to filter low energy X-rays exiting from the source. The commercial software VGStudio MAX from Volume Graphics GmbH [18] that includes beam-hardening correction is used for slice reconstruction and artefact reduction.

*2.2. From the binary representation to a mesh*

Two fundamental strategies can be followed to construct a mesh for a digital sample of a complex, porous matrix. The simplest approach, by which the present results have been obtained, consists in generating an unstructured mesh of cubes, where the computational cells coincide with the void voxels obtained from the X-ray tomography. Figure 1 shows a picture of a sample of metal foam, a digital volume extracted from the sample and a particular of the voxel-based mesh. The voxel size is $81\mu$m.



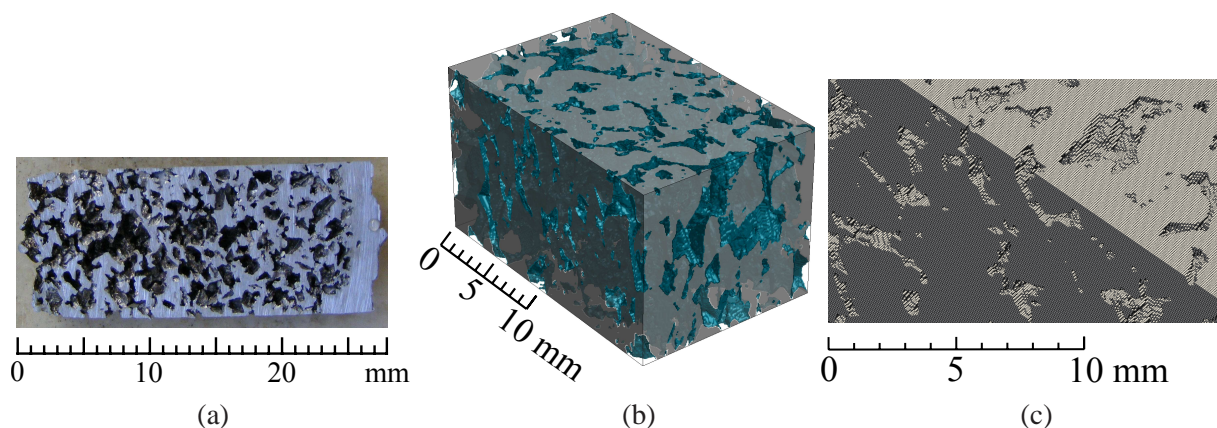**Figure 1.**   (a) Picture of a sample of metal foam; (b) digital volume extracted from the sample $(21.789 \times 14.175 \times 12.798$mm); (c) particular of the voxel-based mesh.

In the second approach, an unstructured, tetrahedral or hybrid mesh is automatically generated once an STL representation of the pore-grain interface is available. Several commercial tools are available, to this end. Some experience has been gained with the +FE module by Simpleware [19], which provides utilities for generating both surface (triangular/quadrilateral) and volume (tetrahedral/hexahedral) meshes.

The voxel-based mesh generation approach presents some distinctive positive features, which are briefly outlined below.

- The fluid-solid interface reconstructed by X-ray tomography is inherently rough and any smoothing operation is arbitrary. The stair-step pattern of the interface represents the real surface roughness with length scale comparable to the voxel size.
- Global and local (by Octree techniques [20]) refinements can be easily achieved by splitting the cubic cells, without affecting the quality of the mesh.
- The mesh generation process is fast and automatic [13].

*2.3. Image processing and morphological analysis*

Sub-volumes of interest of size in excess to $1000^3$ voxels are extracted from the stack of slices. The voxel volumes are treated with non-linear filters to mitigate the noise. The basic median filter with a $3 \times 3 \times 3$ kernel is a good candidate for removing noise whilst preserving edges.

The segmentation of the gray level voxel volume into a boolean tridimensional matrix where the pore space and solid material are represented by 0 and 1 respectively is based on the histogram of the luminosity value of all the voxels. The peaks and valleys in the histogram are used to discriminate between solid and void. The segmentation threshold is placed in the valley. The binary volume obtained is used for pore-space morphological measurements.

Figure 2(a) is a three-dimensional visualization of a sub-volume ($120^3$ voxels) of a sample of sandstone reservoir rock. The iso-surface representing the pore space walls is coloured in red. The material is shown as transparent grey. The pores are left void. The pore space is often sub-divided into pore-bodies that are relatively stubby and the narrow ducts or throats that connect these pores. The individual pores are segmented with a proprietary code that exploits a distance-transform-based (DT hereafter) watershed algorithm. The standard 3D watershed-transform is a parameter-free technique used to resolve pores in an objective manner. It is well known that the standard watershed suffers of severe over-segmentation. Here the pathology is successfully treated with a H-minima transform that suppresses all the local minima regions whose depth is less than a set scalar threshold [21]. In order to accurately calculate three-dimensional gradients, used by the watershed method to identify local minima, the resolution of the original volume is magnified by a factor 5. The segmented pores are visualized in figure 2(b) and their size distribution is shown in figure 2(c).

The medial axis is a path centred with respect to the boundary walls and its length is useful for pore space morphological characterization. As an example, the tortuosity is a morphological indicator of the easiness to pass through a porous media for a size-less particle. According to the most common definition, tortuosity is estimated as the ratio of the mean effective path length through a porous medium to the thickness of the medium or to the linear distance in the media between the start and the end of the particle path. Since one can connect an entrance point to an exit point with many paths, herewith the shortest and largest medial path is considered for tortuosity estimation. Figure 3 shows the path of a particle released at the top side of a tomographic volume with the objective to reach a point at the opposite side. The paths were extracted with a methodology based on the weighted geodesic distance transform [22, 23].
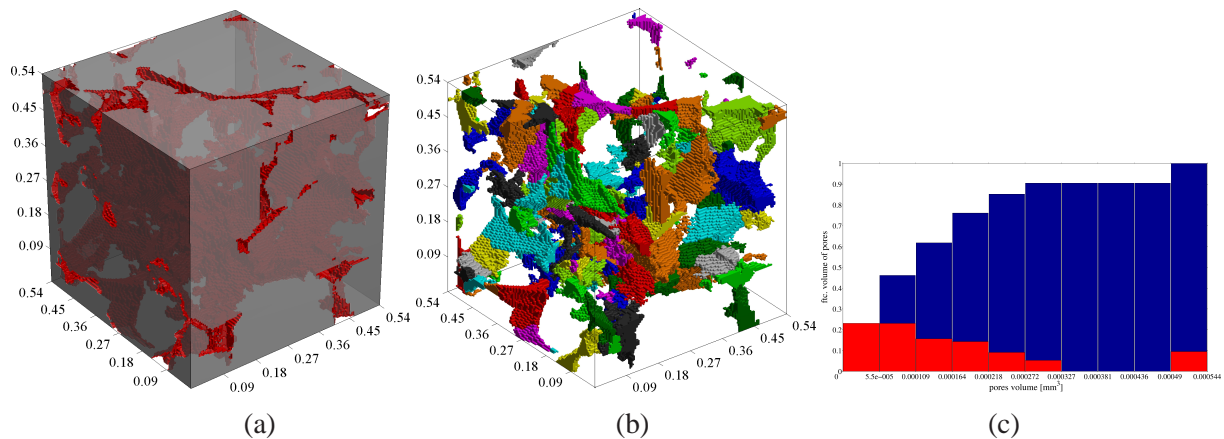
**Figure 2.** (a) Reservoir sample. (b) Segmented pore space. (c) Pore-size distribution (red) and cumulative pore-size distribution (blue). Lengths are expressed in millimetres.
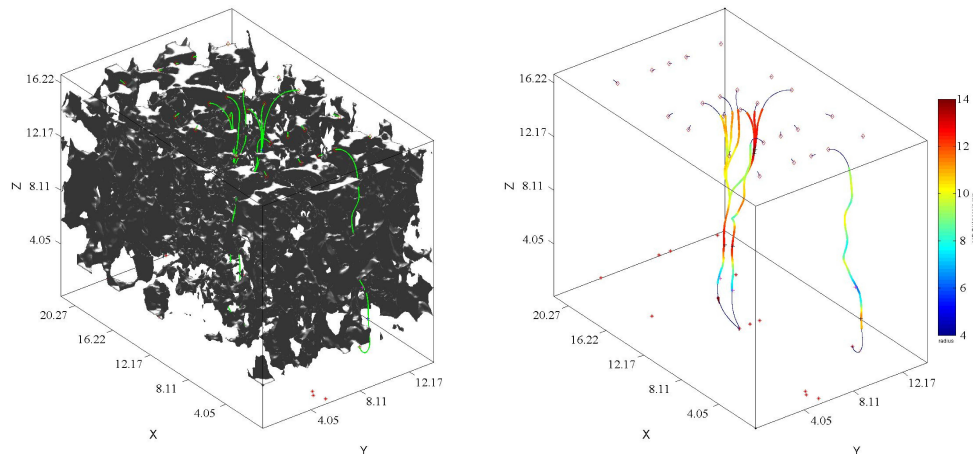


**Figure 3.** Path of a particle released at the top side of a tomographic volume with the objective to reach a point at the opposite side.

### 2.4. Pore-scale fluid dynamics simulation

In the following, the pore-network model [24] for single-phase flow and the Finite Volume method [25] for both single- and two-phase flow are briefly outlined.

*2.4.1. Single-phase, pore-network models*   When a porous medium is synthetically represented as a set of *pores*, the laminar flow through it can be modelled as a linear, hydraulic network. Schena et al. [24] suggest to improve the pore-network modelling approach by taking into account the real shape of the cross-section of the branches, to calculate more reliable hydraulic resistance coefficients. Each branch is represented as a series arrangement of sub-branches with uniform cross-section. Poiseuille flow is assumed in each sub-branch. The specific hydraulic conductance of a sub-branch, $K'$, is defined by the following equation

$$Q = K' \frac{\Delta p}{\rho \, g} \tag{2}$$

where $Q$ denotes the volumetric flow rate, and the hydraulic conductance of the whole branch, $K$, is calculated as:

$$K = \left[ \sum_j \frac{L_j}{K'_j} \right]^{-1} L_{\text{tot}}; \quad L_{\text{tot}} \equiv \sum_j L_j \tag{3}$$

where the index $j$ denotes a specific sub-branch.

Specific hydraulic conductance and absolute permeability are related as follows:

$$K' = \frac{k \, \rho \, g \, A}{\mu \, L} \tag{4}$$

The absolute permeability of three digital samples of sandstone rock, identified as H, M, L, is compared against experimental results in table 1. Laboratory experiments for absolute permeability measurements were carried out in the petro-physical laboratory of an oil company using a high pressure Hassler sleeve core holder. The protocol is detailed in [26].

**Table 1.** Experimental and calculated values of absolute permeability for three samples of sandstone rock.

| Sample | $k \ [m^2 \times 10^{-13}]$ experimental | $k \ [m^2 \times 10^{-13}]$ calculated |
|--------|-------------|------------|
| H | 9.5 | 20.7 |
| M | 1.9 | 4.2 |
| L | 0.39 | 0.14 |

*2.4.2. Single-phase FVM*   As we are only concerned with laminar flow of liquids at very low pore-Reynolds number, the well-known incompressible, steady-state Navier-Stokes equations are solved. Three different types of boundary conditions are enforced on the boundary of the computational domain. No-slip boundary conditions are enforced on the solid-fluid interface, while on the fluid-fluid open portions of the boundary either pressure-inlet or pressure-outlet conditions are enforced. Symmetry conditions are applied on the lateral faces of the sample. The choice of boundary conditions is of course rather arbitrary. Nevertheless, the point here is not to reproduce a flow subject to specific conditions, but rather to compute the transfer function of the porous sample with respect to applied pressure gradients. In this perspective, the enforcement of pressure boundary conditions seems appropriate.

Both the commercial software ANSYS Fluent® [27] and the open-source software OpenFoam® [28] are used to solve the Navier-Stokes equations. Both models adopt a cell-based, co-located discretization approach. The accuracy of the available spatial discretization algorithms ranges between first and fourth-order. In the present, reported applications, second-order upwind schemes for the advective term are preferred for robustness, while the viscous term is discretized by the least-squares or the Gauss methods.

*2.4.3. Multiphase FVM*   Here the finite-volume/volume-of-fluid (FV-VOF) commercial solver ANSYS Fluent® [27] is used for the simulation of the oil/water flow in the pore-space of a sandstone rock that has been reconstructed using high resolution X-ray computed tomography. The VOF is a technique widely used to tackle problems in which two or more fluids are present and the dynamics of the interface is of interest. It was first introduced by Nicols et al. [29]. Various improvements have been developed subsequently and a non-exhaustive list is reported by Tang et al. [30]. Here VOF is used for tracking the shape of the water/oil interface. The phase volume fraction is defined at each computational cell of the

fixed regular and uniform computational grid adopted. The volume fraction function is discontinuous passing through the interface. The piece-wise linear interpolation reconstruction (PLIC) algorithm is used in the present work for interface tracking. The method is coupled with the continuum surface force (CSF) algorithm for surface force modelling that adds a source term in the momentum equation, proportional to the interface curvature [31]:

$$\boldsymbol{F}_{\mathrm{CSF}} = \frac{2\,\rho}{\rho_w + \rho_o}\,\sigma_{w\,o}\,\kappa\,\nabla\,\alpha_w \tag{5}$$

where $\kappa$ denotes the curvature of the oil-water interface, $\sigma_{w\,o}$ the water-oil surface tension, $\alpha_w$ the water volume-fraction and $\rho$ is the volume-averaged mixture density:

$$\rho \equiv \alpha_w\,\rho_w + \alpha_o\,\rho_o \tag{6}$$

Wall adhesion is modelled by assuming a *contact angle* between the fluid-fluid interface and the solid wall. In the *dynamic* boundary condition implemented in ANSYS Fluent$^{\circledR}$ [27], specification of the contact angle is used to adjust the interface curvature near the wall. Pressure-velocity coupling is realized via the pressure-implicit with splitting of operators (PISO) scheme [25]. A single pressure-correction step has been preferred in the present calculations for computational efficiency.

## 3. Results
### 3.1. Calculation of absolute permeability through metal foams and reservoir rocks
*3.1.1. Metal foams*　　An open-cell aluminium foam produced by infiltration casting was examined by X-ray CT [32]. A tomographic scan encompassing $269 \times 175 \times 158$ voxels is used, with resolution $81\mu$m. The porosity of the sample and the mean pore diameter are calculated by image-processing techniques and result in $\epsilon = 79.4\%$ and $d_p = 1.72$mm, respectively. Further details and a through morphological characterization of this material can be found in Boschetto et al. [14, 15], Piller et al. [32]. Figure 4 shows the segmented pores of the aluminium foam of figure 1, coloured with a pallet associated to the pore size. Here the aluminium material is not shown. Avizo Fire$^{\circledR}$ from FEI Visualization Sciences Group [33] is used to separate individual pores with a watershed driven by the DT map.

　　A set of simulations are performed for the sample of metal foam shown in figure 1. The same nature of the infiltration casting process [14] suggests that the inner structure of the considered foam is far from isotropic. Therefore, the fluid intrusion direction is arbitrarily selected as corresponding to the mean flow direction of molten aluminium during casting. The range of pore-scale Reynolds number, $\mathrm{Re}_p \equiv U_D\,d_p/\nu_f$, is selected in order to investigate the Darcy and the Darcy-Forchheimer flow regimes, see table 2.

　　A common correction to the Darcy model, aimed at extending its range of validity to the laminar inertial regime $\mathrm{Re}_p \lesssim 100$, adds a quadratic term, yielding the Darcy-Forchheimer model [34, 35] in non-dimensional form:

$$\mathrm{C_D} = \frac{1}{\mathrm{Re}_p\,\mathrm{Da}} + \frac{C_E}{\sqrt{\mathrm{Da}}} \tag{7}$$

The Darcy number Da and the drag coefficient $\mathrm{C_D}$ are defined as follows

$$\mathrm{Da} = \frac{k}{(d_p)_L^2}; \qquad \mathrm{C_D} = -\frac{\Delta p_f\,(d_p)_L}{\rho_f U_D^2\,L_x} \tag{8}$$

The Darcy number and the Ergun coefficient for the present sample are calculated by linear regression with equation (7), yielding:

$$\mathrm{Da} \; = \; 2.757 \times 10^{-2} \pm 4.2 \times 10^{-4}; \quad C_E \; = \; 1.566 \times 10^{-1} \pm 4.1 \times 10^{-3} \tag{9}$$
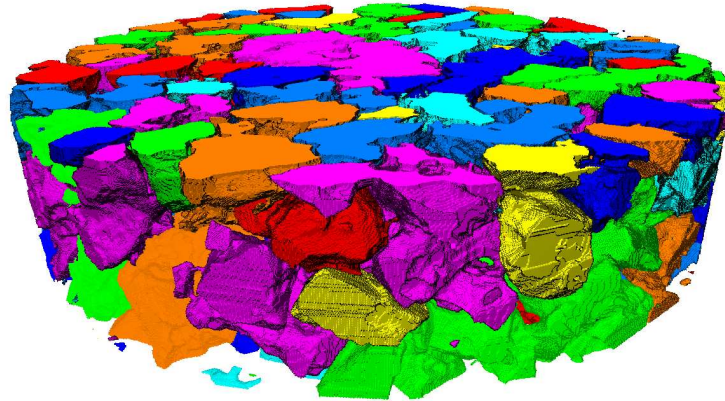
**Figure 4.** The segmented pores coloured with a pallet associated to the pore size. Here the aluminium material is not shown.

where the $95\%$ confidence bounds are also reported. The absolute permeability of the sample can be directly derived from the Darcy number and the mean pore diameter:

$$k = 8.2 \times 10^{-8} \text{ m}^2 \tag{10}$$

**Table 2.** Drag coefficient calculated at different pore-scale Reynolds numbers.

| Case | A | B | C | D | E | F | G | H |
|------|-------|-------|-------|------|-------|-------|-------|-------|
| $Re_p$ | 0.61 | 1.22 | 3.04 | 6.08 | 12.17 | 30.42 | 45.00 | 60.83 |
| $(C_D)$ | 67.95 | 34.18 | 14.12 | 7.57 | 4.33 | 2.39 | 1.97 | 1.75 |

*3.1.2. Reservoir rocks* The full tensor of absolute hydraulic permeability is estimated for a sample of sandstone reservoir rock from a deep oil exploration and compared with laboratory experimental measurements. The rock porosity is estimated about $11\%$ by image-processing techniques. Further morphological details can be found in Piller et al. [36]. The spatial resolution of the tomographic scan is $4.5\,\mu$m. The numerical simulations are carried out on a sub-volume encompassing $600^3$ voxels. Comparison of morphological parameters against a $1.5\,\mu$m tomographic model of the same sample, scanned at the ID19 line of ESRF synchrotron at Grenoble (France), does not show significant discrepancies. The proposed methodology is validated by reproducing literature results on mono-disperse periodic arrays of spheres.

The hydraulic permeability tensor is positive-definite and symmetric [35]. In this study the full permeability tensor is estimated, by applying three sets of pressure gradients to the porous sample and computing the resulting specific discharge $q$. With three experiments, nine equations are derived:

$$-\frac{1}{\mu}\sum_{j=1}^{3} k_{ij} \frac{\partial p^{(k)}}{\partial x_j} = q_i^{(k)} \tag{11}$$

where the superscript denotes a particular experiment. As in each experiment only a single component of the pressure gradient is non-zero, the following system of equations is obtained:

$$
-\frac{1}{\mu}
\begin{pmatrix}
\frac{\partial p^{(1)}}{\partial x} & 0 & 0 & 0 & 0 & 0 \\
0 & \frac{\partial p^{(1)}}{\partial x} & 0 & 0 & 0 & 0 \\
0 & 0 & \frac{\partial p^{(1)}}{\partial x} & 0 & 0 & 0 \\
0 & \frac{\partial p^{(2)}}{\partial y} & 0 & 0 & 0 & 0 \\
0 & 0 & 0 & \frac{\partial p^{(2)}}{\partial y} & 0 & 0 \\
0 & 0 & 0 & 0 & \frac{\partial p^{(2)}}{\partial y} & 0 \\
0 & 0 & \frac{\partial p^{(3)}}{\partial z} & 0 & 0 & 0 \\
0 & 0 & 0 & 0 & \frac{\partial p^{(3)}}{\partial z} & 0 \\
0 & 0 & 0 & 0 & 0 & \frac{\partial p^{(3)}}{\partial z}
\end{pmatrix}
\begin{pmatrix}
k_{11} \\
k_{12} \\
k_{13} \\
k_{22} \\
k_{23} \\
k_{33}
\end{pmatrix}
=
\begin{pmatrix}
q_1^{(1)} \\
q_2^{(1)} \\
q_3^{(1)} \\
q_1^{(2)} \\
q_2^{(2)} \\
q_3^{(2)} \\
q_1^{(3)} \\
q_2^{(3)} \\
q_3^{(3)}
\end{pmatrix}
\tag{12}
$$

This means that in the first experiment the west face of the computational domain is a pressure inlet, while all other open boundary surfaces are classified as pressure outlets, with analogous arrangements for the second and third experiments.

The computed principal permeabilities are compared against the experimental measurement, the Kozeny-Carman correlation and the hydraulic network result [37] in table 3. Both the computed results and the Kozeny-Carman correlation overestimates the experimental measurement. As for the numerical results, this difference could be ascribed either to macroscopic inhomogeneities in the sample used in the experiments, or to insufficient resolution in the tomographic reconstruction, or to the inadequacy of the computational domain as a *representative elementary volume* (REV) [35].

**Table 3.** Computed principal components of the hydraulic permeability tensor, in $m^2 \times 10^{-13}$, for the real porous sample [36].

| | | |
|---|---|---|
| $k_{\mathrm{I}}$ | | 2.4 |
| $k_{\mathrm{II}}$ | | 2.7 |
| $k_{\mathrm{III}}$ | | 3.0 |
| $k_{\exp}$ | | 1.9 |
| $k_{\text{Kozeny-Carman}}$ | $(M_s\,\mathrm{cm}^2/\mathrm{cm}^3)$ | 7.0 (207) |
| $k_{\text{netw}}$ | | 4.2 |

### 3.2. Calculation of relative permeability through reservoir rocks

The major factors affecting relative permeability are pore structure, flow conditions, saturation history and wettability. However, for a given medium, the relative permeability is commonly assumed to be saturation-dependent only. Here the interest is to reproduce the steady-state method numerically,

characterizing via relative permeability curves the dynamics of a two-phase (oil/water) flow within the digital sample of sandstone rock reconstructed by micro-CT, shown in figure 2(a). The pore-scale simulations are carried out using a $200^3$ sub-volume extracted from the whole tomographic scan. The considered fluid properties are:

$$\rho_w \quad = \quad 998.2 \text{ kg/m}^3 \quad ; \quad \mu_w \quad = \quad 0.001 \text{ kg/m s}$$

$$\rho_o \quad = \quad 800.0 \text{ kg/m}^3 \quad ; \quad \mu_o \quad = \quad 0.003 \text{ kg/m s}$$

$$\sigma_{w,o} \quad = \quad 0.05 \text{ N/m} \quad ; \quad \theta_{w,o} \quad = \quad 30°$$

where $\rho$ and $\mu$ denote density and dynamic viscosity of the fluids, $\sigma_{w,0}$ is the surface tension and $\theta_{w,o}$ is the equilibrium contact angle.

Once the digital domain is obtained the flow simulation can be carried out. The mixture velocity is imposed at the sample's inlet while the static pressure is enforced at the outlet. In turn, the latter condition implies zero capillary pressure at outlet, a boundary condition that is commonly used in special core analysis simulations. Oil and water volume ratio at the inlet section are fixed. The water layer covers the pore surface, while the oil fills the core of the pore body. Thus, at the fluid inlet section of the meshed pore-space, specialized image-processing tools are used to identify the boundaries of the pores and to adjust the thickness of the water layer according to the prescribed water/oil volumetric ratio. The zero-velocity (*no-slip*) condition is applied at the pore-fluid interface. The applied boundary conditions are summarized in table 4. The sample is initially filled with water. Once reached the stationary conditions, in terms of oil saturation $S_o$ and pressure, the relative permeabilities for both oil, $k_{r,o}$ and water, $k_{r,w}$, are obtained using their definitions:

$$\boldsymbol{q}_o = -\frac{k\,k_{r,o}}{\mu_o}\,\nabla p_o \qquad \boldsymbol{q}_w = -\frac{k\,k_{r,w}}{\mu_w}\,\nabla p_w \tag{13}$$

The water and oil saturations are defined as:

$$S_o \equiv \frac{\text{volume of oil into pore space}}{\text{volume of pore space}} \qquad S_w \equiv 1 - S_o \tag{14}$$

Each test provides a couple of points in the relative oil and water permeability curves. The complete curves can be derived by changing oil/water injection ratio and measuring the microscopic variables when fluid saturation reaches equilibrium. The simulated data are fitted with the empirical relation proposed by Brooks and Corey and further compared to the experimental data obtained from a larger sample of the same rock using laboratory waterflood data [26]. Figure 5(a) shows two sets of data concerning oil (red) and water (blue). The circles represent relative permeabilities calculated with the numerical simulation, the dashed lines the fitting curves, the triangles the experimental data. Figure 5(b) shows a snapshot of the displacement process within the porous domain, where the oil phase is represented in red while the water phase appears in transparent blue.

Analysing the diagram and comparing the curves, it is possible to conclude that the simulated data are in good agreement with the experimental data, referring to the water; on the other hand, a discrepancy between the two sets of data for the oil is undeniable. The reasons of this difference are ascribable to the different dimensions of the samples used for the characterization: a one inch in diameter core plug for the laboratory experiment and a $200^3$ voxels cube of side 1 mm for the numerical simulations. The simulation is carried out with fluid velocities lower than those recorded in the laboratory experiment in order to grant pore-Re numbers typical of a laminar flux.

**Table 4.** Boundary conditions used in the two-phase flow simulations.

| Boundary | Condition |
|---|---|
| Inlet | Velocity inlet; $\alpha_o$ assigned |
| Outlet | Pressure outlet; either $\alpha_o = 1$ (imbition) or $\alpha_w = 1$ (drainage) assigned to recirculating fluid |
| Pore/rock interface | No-slip condition; wall adhesion specified through static contact angle. |

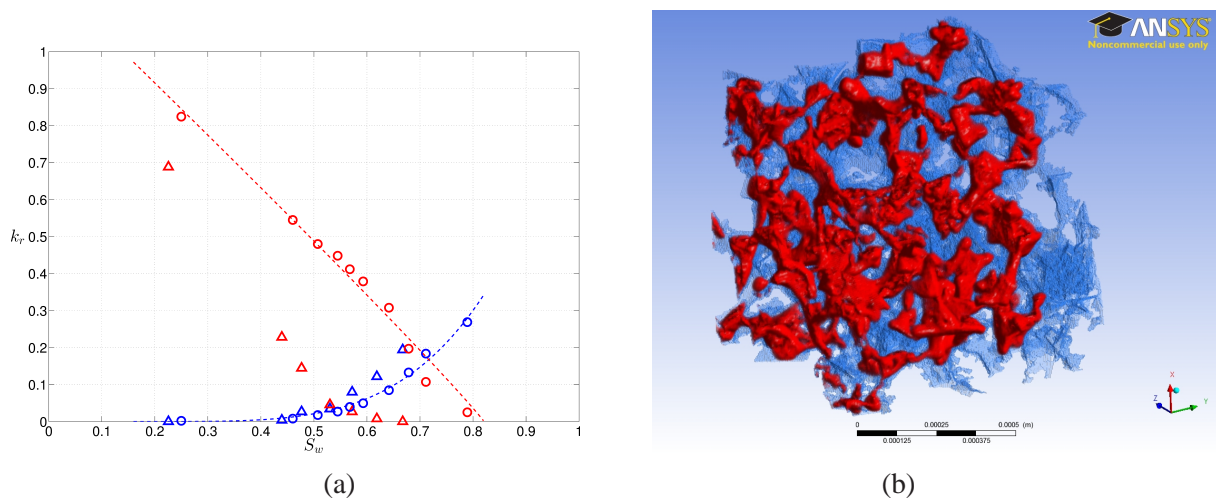

(a)                                (b)

**Figure 5.** (a) Two sets of data concerning oil (red) and water (blue). The circles represent relative permeabilities calculated with the numerical simulation, the dashed lines the fitting curves, the triangles the experimental data. (b) Instantaneous visualization of oil phase (red) distribution within the pore space, initially filled with water (transparent blue).

## 4. Concluding remarks

The combined use of micro-CT systems, image analysis tools, volume meshing codes and CFD software allows reconstructing the complex morphology of the pore space of porous media and investigating their flow properties. This paper gives a thorough presentation of the work-flow to be used for predicting flow properties in both single- and multi-phase flows by pore-scale numerical simulation. The proposed methodology is used to evaluate the single-phase flow properties of a metallic foam, the full tensor of hydraulic permeability and the pressure induced and capillary driven multiphase flow of a sample of reservoir rock. Synthetic indicators such as absolute permeability, relative permeability and residual irreducible saturation can be computed on small samples rather than with costly and time consuming laboratory experiments.

## References

[1] Loomis A G and Crowell D C 1962 *USBM Bulletin* **599**

[2] Akin S 2001 *J Petrol Sci Eng* **30**(1) 1

[3] Kho J C Y and Stevens R L 1975 *J Heat Transf* **97** 309

[4] Bai M and Chung J N 2011 *Int J Therm Sci* **50**(6) 869

[5] DeGroot C T, Straatman A G and Betchen L J 2009 *J Electron Packag* **131**(2) 021001

[6] Zong Y, Zhou B and Sobiesiak A 2006 *J Power Sources* **161** 143

[7] Faubion J M 2007 Ph.D. thesis Louisiana State University

[8] Benedik G, Širok B, Markič I and Eberlinc M 2011 *Heat Mass Transfer* **47**(6) 679

[9] Mostaghimi P, Bijeljic B and Blunt M J 2012 *SPE Journal* (**17**)(4) 1131

[10] Mostaghimi P, Blunt M J and Bijeljic B 2013 *Math Geosci* (**45**)(1) 103

[11] Boomsma K, Poulikakos D and Ventikos Y 2003 *Int J Heat Fluid Fl* **24** 825

[12] Krishnan S, Murthy J Y and Garimella S V 2006 *J Heat Transf* **128** 793

[13] Gerbaux O, Buyens F, Mourzenko V V, Memponteil A, Vabre A, Thovert J F and Adler P M 2010 *J Colloid Interf Sci* **342** 155

[14] Boschetto A, Costanza G, Quadrini F and Tata M E 2007 *Mater Lett* **61**(14-15) 2969

[15] Boschetto A, Campana F, Giordano V and Pilone D 2012 *Computational Modelling of Objects Represented in Images: Fundamentals, Methods and Applications III - Proceedings of the International Symposium, CompIMAGE* (*Rome, Italy*)

[16] Radon J and Parks P C 1986 *IEEE T Med Imaging* **5**(4) 170

[17] Feldkamp L A, Davis L C and Kreiss J W 1984 *J Opt Soc Am A* **1** 612

[18] VGStudio MAX from Volume Graphics GmbH, http://www.volumegraphics.com/en/

[19] +FE module by Simpleware, http://www.simpleware.com/

[20] Samet H 2006 *Foundations of multidimensional and metric data structures* Morgan Kauffman Publishers (San Francisco, USA)

[21] Soille P 1999 *Morphological Image Analysis: Principles and Applications* Springer-Verlag (Berlin)

[22] Deschamps T and Cohen L D 2001 *Med Image Anal* (**5**)(4) 281

[23] Peyré G and Cohen L 2005 *Heuristically driven front propagation for geodesic paths extraction. Lecture Notes in Computer Science* Springer-Verlag GmbH (Berlin)

[24] Schena G, Radaelli F, Piller M, Favretto S and Rossi E 2008 *Society of Petroleum Engineers - 70th European Association of Geoscientists and Engineers Conference and Exhibition* (*Rome, Italy*)

[25] Ferziger J H and Perić M 1972 *Computational Methods for Fluid Dynamics. 3$^{rd}$ ed.* Springer (Berlin, Germany)

[26] Tiab D and Donaldson E C 2004 *Petrophysics 2$^{nd}$ ed. - Theory and Practice of Measuring Reservoir Rock and Fluid Transport Properties* Elsevier (New York, USA)

[27] ANSYS Inc. 2010 *ANSYS FLUENT Theory Guide*

[28] OpenFoam website, http://www.openfoam.com/

[29] Nichols B D and Hirt C W 1981 *J Comp Phys* (**39**)(1) 201

[30] Tang H, Wrobel L C and Fan Z 2004 *Comput Mater Science* (**29**) 103

[31] Brackbill J U, Kothe D B and Zemach C 1992 *J Comp Phys* (**100**) 335

[32] Piller M, Boschetto A, Stalio E, Schena G and Errico O 2013 *J Porous Media* (**16**)

[33] Avizo Fire from FEI Visualization Sciences Group, http://www.vsg3d.com/

[34] Scheidegger A E 1960 *The physics of flow through porous media* University of Toronto Press (Toronto, CA)

[35] Bear J 1972 *Dynamics of Fluids in Porous Media* Dover Publications (New York, USA)

[36] Piller M, Schena G, Nolich M, Favretto S, Radaelli F and Rossi E 2009 *Transport Porous Med* (**80**)(1) 57

[37] Schena G and Favretto S 2007 *Transport Porous Med* (**70**)(2) 181